Supplementary Information

Delineating the Stepwise Millisecond Allosteric Activation Mechanism of the Class C GPCR Dimer mGlu5

Mingyu Li[1,2,†], Xiaobing Lan[2,†], Xinchao Shi[1], Chunhao Zhu[2], Xun Lu[1], Jun Pu[3], Shaoyong Lu[1,2,*] and Jian Zhang[1,2,*]

[1]State Key Laboratory of Medical Genomics, National Research Center for Translational Medicine at Shanghai, Medicinal Chemistry and Bioinformatics Center, Ruijin Hospital, Shanghai Jiao Tong University School of Medicine, Shanghai 200025, China

[2]Key Laboratory of Protection, Development and Utilization of Medicinal Resources in Liupanshan Area, Ministry of Education, Peptide & Protein Drug Research Center, School of Pharmacy, Ningxia Medical University, Yinchuan 750004, China

[3]Department of Cardiology, Renji Hospital, Shanghai Jiao Tong University School of Medicine, Shanghai 200120, China

[†]These authors contributed equally.

[*]To whom correspondence should be addressed:

Dr. Shaoyong Lu

E-mail: lushaoyong@sjtu.edu.cn

Dr. Jian Zhang

E-mail: jian.zhang@sjtu.edu.cn

Table of Contents

S1. Supplementary Notes

Supplementary Note 1. Convergence test for the partial NEB

Supplementary Note 2. Convergence test for free energy landscapes

Supplementary Note 3. Validation of the MSM

Supplementary Note 4. The loosely coupled dynamics of VFT and 7TM domains

Supplementary Note 5. Glutamate dynamic binding poses in macrostates

Supplementary Note 6. CRD dynamics among simulations

Supplementary Note 7. PAM CDPPB enhances mGlu5 activation via conformational bias

Supplementary Note 8. Mechanistic insights into the full activation of mGlu5 upon G_q coupling

S2. Supplementary Figures and Tables

S3. Supplementary References

S1. Supplementary Notes

Supplementary Note 1. Convergence test for the partial NEB

To assess the convergence and quality of the minimum energy path (MEP) generated by NEB, we conducted a convergence test by altering the number of interpolated images (i.e., 16, 24, 32 and 40). The results demonstrate that employing 16 images leads to sporadic coverage of the transition pathway, whereas using more than 24 images ensures a more complete and consistent exploration (Supplementary Figure 1). Our findings suggest that 32 images might offer an optimal compromise between computational efficiency and thorough pathway investigation. Furthermore, we conducted a systematic survey of the literature on the application of the NEB technique in biomolecular simulations. Representative studies involving monomeric proteins, polymeric proteins, and protein-DNA systems[1-6]. All these studies preferred using between 22 and 32 images for exploring the MEP, successfully generating a reliable MEP for subsequent mechanism investigations. Consequently, our choice of 32 images for investigating the activation pathway of the dimeric mGlu5 receptor is both sufficient and well-supported by existing research practices.

Supplementary Note 2. Convergence test for free energy landscapes

To confirm that the subsequent extensive MD samplings are sufficient for a converged free energy landscape and transition pathway, we designed a convergence test by projecting the varied subsets of the MD conformations onto the two slowest tICs (Supplementary Figure 2, A: 0.2 μs × 130, B: 0.4 μs × 130, C: 0.6 μs × 130, D: 0.8 μs × 130, E: 1.0 μs × 130). All subsets show a highly similar conformational distribution, notably without the emergence of new metastable regions in the phase space as conformational sampling increased, confirming that the MD samplings are enough to explore the activation pathway of mGlu5.

Supplementary Note 3. Validation of the MSM

Firstly, we determined features to properly describe the slowest dynamics associated

with the inter-subunit rearrangement of mGlu5. Not only the aligned Cartesian coordinates but also various distance features were incorporated. The distance features were obtained by varying the heavy atom pairs between protomers in the active cryo-EM structure within a range of cutoffs. To incorporate as many distances as possible, nine cutoffs were considered, ranging from 7 to 15 Å, which yielded distance pairs ranging from 1,274 to 119,359. Finally, the closest heavy-atom distances between each pair of residues were calculated, denoted as $f(d) = \min(d)$, and we also applied an inverse transformation ($f(d) = d^{-1}$). These nineteen different feature types were evaluated by using the VAMP2 score across five lag times (2 ns, 5 ns, 10 ns, 15 ns, 20 ns) using the top ten eigenvalues and five-fold cross-validation (Supplementary Figure 3A). The scores suggetsed that these feature types yield MSMs of comparable quality. For distance features, the choice of distances of a 13 Å cutoff (totaling 58,848) proved effective, as the introduction of additional atom pairs beyond this cutoff did not have substantial improvement. It suggests that the atom pairs within this range could sufficiently describe the slowest conformational dynamics. However, the aligned Cartesian coordinates achieved the highest mean VAMP2 score, thereby justifying this feature type as the most suitable for MSM construction.

The justified features were projected via tICA to capture the slow dynamic processes and construct the MSM. More importantly, the GMRQ algorithm was used to select hyperparameters for the MSM[7,8]. The GMRQ score, determined through 5-fold cross-validation, indicated that utilizing the 2 slowest tICs and 300 microstates adequately represents the Markov model (Supplementary Figure 3B). The inclusion of more than 5 tICs and 500 microstates could lead to overfitting. Therefore, the 2 slowest tICs were clustered into 300 microstates using the K-means clustering algorithm to build the MSM.

Next, to select an appropriate memoryless lag time for the MSM, we performed the implied timescale test, which estimated a series of transition probability matrices (TPMs) across all microstates at varying lag times. The implied timescale is determined from TPM according to Eq. (S1):

$$\tau_i = -\frac{\tau}{ln\lambda_i} \quad \text{(S1)}$$

In this equation, τ stands for the lag time used for calculating the TPM, λ_i equals the i^{th} eigenvalue of the TPM and τ_i is the implied timescale corresponding to the i^{th} implied mode of the system. As a function of the lag time τ, τ_i will be constant when the transition dynamics between microstates are memoryless, or Markovian. By plotting the implied timescales, our τ_i appear to coverage from a lag time than 10 ns (Supplementary Figure 3C).

According to the shape of the mGlu5 activation landscape, the 300 microstates were further clustered into 5 macrostates using the PCCA+ algorithm (Supplementary Figure 3D). The five macrostates were well separated on the landscape and were validated by the Chapman-Kolmogorov test (Supplementary Figure 3E).

Supplementary Note 4. The loosely coupled dynamics of VFT and 7TM domains

It is widely recognized that in monomeric β_2-adrenergic receptor, the ligand-binding site is loosely coupled to the connector, which in turn is loosely coupled to the G-protein-binding site[9,10]. Similar loose couplings were observed in the dimeric, multidomain mGlu2 receptor between the VFT domains (ligand-binding site) and the CRDs (connector), as evidenced by smFRET spectroscopy[11]. Our simulations extended these observations by revealing loosely coupled dynamics not only between the VFT domains and CRDs (R2 = 0.62) but also between the CRDs and the 7TM domains (G protein-binding site, R2 = 0.58). This contrasted with the tighter coupling observed between the VFT and the B2' module of CRDs (R2 = 0.91), which are linked by inter-domain disulfide bonds (Supplementary Figure 4). The three functionally relevant regions of mGlu5—VFT domains, CRDs, and 7TM domains—appear to be loosely coupled to one another. These results suggested that such loose coupling could represent a general mechanism of allosteric regulation across both monomeric and dimeric GPCRs. Of note, the loose correlation between the movements of CRDs and 7TM domains across protomers indicated that CRD conformation might not be a super robustness indicator for the activation state of mGlu5 receptors.

Supplementary Note 5. Glutamate binding poses in metastable states

Crystallographic studies have established the conserved binding pose of glutamate in mGlu receptors. Despite this, the dynamic processes that underpin glutamate binding are not well understood. One MD simulation study of drug binding to GPCRs has shown that drugs can initially bind in non-crystallographic poses before transitioning to the crystallographic pose[12]. Similar dynamic behavior has also been observed for glutamate binding. It can assume the non-crystallographic, inverted poses in various glutamate-binding systems, including the ionotropic glutamate receptors (i.e., GluA2 of the AMPA receptor and GluN2A of the NMDA receptor), and periplasmic binding proteins (i.e., ligand-bound glutamine binding protein[13-15]. Very recently, Cannone et al. discovered an intermediate and transient binding pose of quisqualate (a glutamate analogue) in a mGlu5 cryo-EM structure[16]. The quisqualate was found to only form polar interactions with D305 and S173, diverging from the classical binding pose, which typically involves polar interactions with the conserved residues Y64, S152, T175, and K396.

Consistently, our simulations further revealed that glutamate could initially bind in a transient, non-crystallographic pose, eventually transitioning to the crystallographic pose in mGlu5 (Supplementary Figure 5). In the initial S1 state, glutamate's binding pose was inverted. In protomer A, the α-carboxylate of glutamate interacted with the side chains of R68, S173 and K396, whereas its γ-carboxylate interacted with the side chains of S42, W100 and S151. In protomer B, its α-carboxylate made polar contacts with the side chains of R68 and K396, while the γ-carboxylate contacted the side chains of Q46 and R61. This inverted binding was partially maintained in the subsequent S2 state, where the α-carboxylate of glutamate contacted the side chains of R68 and K396 in protomer A and R310 in protomer B, interactions typically formed with the γ-carboxylate in the available crystallographic structures. Eventually, the glutamate began to adopt the classic binding mode, with its α-carboxylate coordinating with S152 and T175 and γ-carboxylate forming polar contacts with Y64 and K396 (in S2') and

R310 (in S3).

These observations from our simulations, in conjunction with data from prior studies, do not contradict the energetically favorable classical crystallographic binding modes of glutamate. Rather, it simply suggests the possibility of an alternative or dynamic binding pose, which also indicates a significant degree of dynamism within the VFT domains.

Supplementary Note 6. CRD dynamics among simulations

To investigate the module-specific mobility within simulations, we calculated the per-residue root-mean-square fluctuations (RMSF) for all heavy atoms of the CRD in both protomers. Notably, the B2' module (highlighted in the orange shade) showed significantly higher fluctuations than the two A1 modules (purple shade) within the CRDs (Supplementary Figure 6A). Furthermore, we employed the DSSP algorithm to assess the stability of the CRDs' secondary structures. The output secondary structure classification of each residue among simulations was shown in Supplementary Figures 6B and C. Consistent with the RMSF analysis, a greater number of secondary structure transitions, specifically from β-sheet to coil, were observed in the B2' module. These observations underscore the highly dynamic nature of the B2' module, potentially indicating its distinct role in the mGlu5 activation.

Supplementary Note 7. PAM CDPPB enhances mGlu5 activation via conformational bias

The mGlu5 receptor is a promising therapeutic target for neural system disorders[17-19]. Positive allosteric modulators (PAMs) that bind to its 7TM regions can enhance receptor activation, potentially offering benefits in the treatment of schizophrenia and cognitive disorders. Remarkably, during the peer review process, several cryo-EM structures of the full-length, active mGlu5 receptor bound to different PAMs were determined, highlighting numerous crucial activation switches for mGlu5, including Y659$^{3.44}$, T781$^{6.46}$, W785$^{6.50}$, F778$^{6.53}$, S809$^{7.3916}$. Among these, the structure of mGlu5

in complex with PAM CDPPB has been released (PDB ID: 8TAO). To delve deeper into how the PAM impacts the dynamics of the mGlu5 activation, we leveraged this structure to conduct unbiased all-atom MD simulations on full-length mGlu5 system bound with glutamate and CDPPB (1 μs × 10 independent MD simulations referencing PDB ID: 8TAO).

Compared to the system where only agonists were added (1 μs × 10 independent MD simulations referencing PDB ID: 6N51), the CDPPB-bound protomer exhibited an outward movement of TM6, decreasing the TM6-TM6 distance and likely leading to a more compact TM6-TM6 interface (Supplementary Figure 15A). To quantify this, we calculated the interaction free energy between the 7TMs employing the molecular mechanics/generalized Born surface area (MM/GBSA) method[20]. The inclusion of CDPPB significantly strengthens the interaction at the 7TM dimer interface, with an interaction energy of -16.8 ± 7.3 kcal/mol compared to -2.5 ± 4.9 kcal/mol in the absence of CDPPB (Supplementary Figure 15B). This result validated a more stabilized active 7TM interface in the presence of CDPPB.

Utilizing Bimane fluorescence, Kumar et al.[21] observed a notable conformational change in the ICL2 upon the addition of CDPPB, distinguishing this effect from that observed with the agonist alone. Although the sensor revealed discrete conformations of ICL2 upon PAM binding, it did not resolve ICL2 structural compositions. Therefore, we generated the conformational landscape of ICL2 from the extensive simulation trajectories (1 μs × 10 repeats × 15 systems). It unveiled that ICL2 existed in a dynamic equilibrium, fluctuating between “closed” or “collapse” states that may occlude the intracellular cavity, and “open” or “extended” states that could facilitate receptor-effector interactions and promote receptor activation (Supplementary Figure 15C and D). The presence of glutamates alone failed to significantly affect this equilibrium, suggesting that orthosteric agonists by themselves were insufficient to stabilize an active ICL2 conformation. In contrast, the addition of CDPPB, or CDPPB in combination with G_q to the glutamate-bound mGlu5, markedly shifted the equilibrium toward an active ICL2 state, characterized by an appropriately open and extended

conformation. Consequently, we proposed that PAM binding transitioned ICL2 from inactive closed or collapsed states, which might impede G_q protein binding, to active open and extended states.

These findings collectively demonstrated that CDPPB exerted its positive allosteric modulation effect on mGlu5 by stabilizing not only the active inter-domain 7TM interface but also the intra-domain ICL2 conformation.

Supplementary Note 8. Mechanistic insights into the full activation of mGlu5 upon G_q coupling

As of now, the structure of the G protein-coupled mGlu5 complex has not been discovered, leaving the full activation mechanisms of mGlu5 largely unexplored. In general, mGlu5 couples with G_q protein. To bridge this gap, we employed Alphafold2-multimer[22,23] to generate the structure of mGlu5-G_q complexes. To simplify the prediction process and highlight the significant interaction regions (mainly involving the α5 helix), we opted for the mini-G_q protein sequence due to its small size[24]. The highest-ranked predicted structure seemed reasonable, evidenced by the high confidence scores of most residues and a similar G_q insertion mode compared to the recently released CASR-G_q cryo-EM structures (Supplementary Figure 16A)[25,26]. Next, we aimed to further enhance the reliability of the predictive mGlu5-G_q complex model by leveraging the just available high-quality crystal structures of the mGlu5 homodimer. The relative position of mGlu5 and downstream mini-G_q was preserved, and the object GPCR was aligned to the most representative active structure of the mGlu5 receptor (PDB ID: 8TAO), referred to all Cαs in the object GPCR. This alignment was refined over five cycles using the Executive RMS function in PyMOL. Following this, the fully active mGlu5 structure, bound with glutamate, CDPPB, and mini-G_q, underwent further refinement by extensive minimization cycles until convergence was achieved. Eventually, 10 independent classical MD simulations, each lasting 1.0 μs, were performed on this refined, fully active mGlu5 structure.

To explore detailed interaction variations at the mGlu5-7TM-G_q interface, we

carried out tICA focusing on the interface contacts. An interface contact was defined as any pair of residues on the mGlu5-7TM and those on the G_q protein, with a closest distance threshold set at 5 Å. The resulting FEL (Supplementary Figure 16C) established by the first two tICs revealed three predominant interaction modes (< 0.5 kcal/mol, labeled G1, G2, G3). A notable conformational shift observed is the tilting of the α5 helix, which exhibited a maximum tilt of approximately 23.3° in G3 compared to its orientation in G1 (Supplementary Figure 16D). Such conformational changes of the α5 helix are also captured in the formation of the fully active NTSR1-G_{i1} and β_2AR-G_s complexes[27,28].

Consistently, the G1 state appeared to be a pre-coupled G_q binding mode, exhibiting minimal insertion into the cavity. This state retained the two key inactivation-stabilizing 'ionic-lock' motifs: a salt bridge between K665$^{3.50}$ and E770$^{6.35}$, and a hydrogen bond between R668$^{3.53}$ and S614$^{2.35}$. Accordingly, the binding energy for G1, as determined through the MM/GBSA method, is the least favorable, approximately -46.8±13.2 kcal/mol (Supplementary Figure 16B and E). In contrast, the G3 state likely represented a fully activated conformation, wherein the ionic-lock motifs were completely disrupted. Moreover, the active-state asymmetric TM6-TM6 interface was formed, with an upward shift in TM6 of the G_q-coupled protomer facilitating the rearrangement of ICL3. This conformational rearrangement orchestrated the cytoplasmic tip of TM3, ICL2 and H8 (potentially the C terminus) to envelop the G_q α5 helix. Owing to these comprehensive interactions (Supplementary Figure 16F), the G1 binding mode was the most energetically favorable (-86.3±17.4 kcal/mol). In addition, the α5 helix formed moderate interaction networks with the 7TM domain in G2, resulting in a binding energy of -68.9±15.7 kcal/mol. Therefore, G2 may represent an intermediate state along the full activation pathway for mGlu5-G_q.

S2. Supplementary Figures and Tables

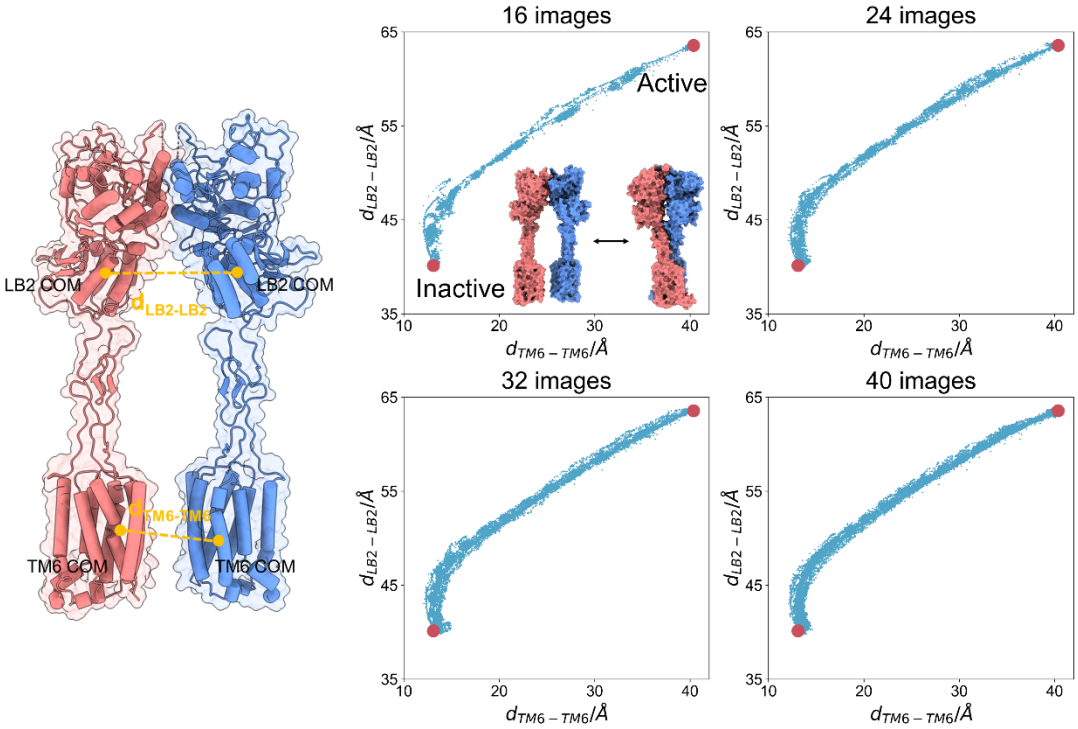

Supplementary Figure 1. Partial NEB calculations were conducted in explicitly solvated systems using 16, 24, 32, and 40 images to examine the convergence of the transition pathway.

In each panel, the red circles are the endpoints of the cryo-EM structures of mGlu5 while blue circles represent simulation snapshots captured at intervals of 10ps.

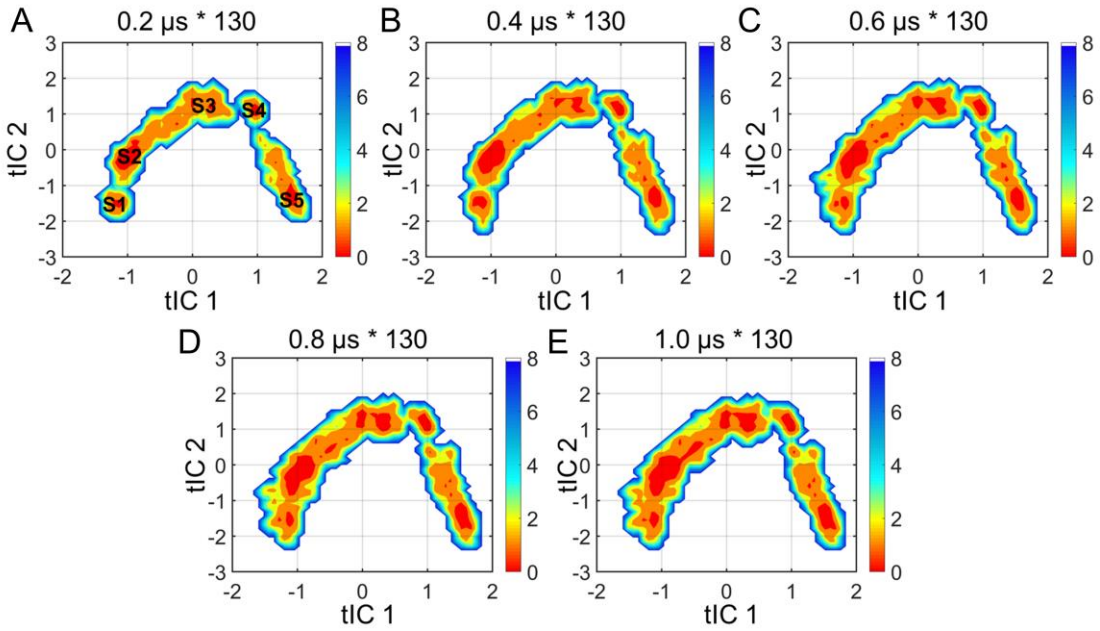

Supplementary Figure 2. Convergence of the free energy landscape and transition pathway was validated by projecting the varied subsets of the MD conformations (aggregated time of 26μs (A), 52μs (B), 78μs (C), 104μs (D), 130μs (E)) onto the two slowest tICs (unit in kcal/mol).

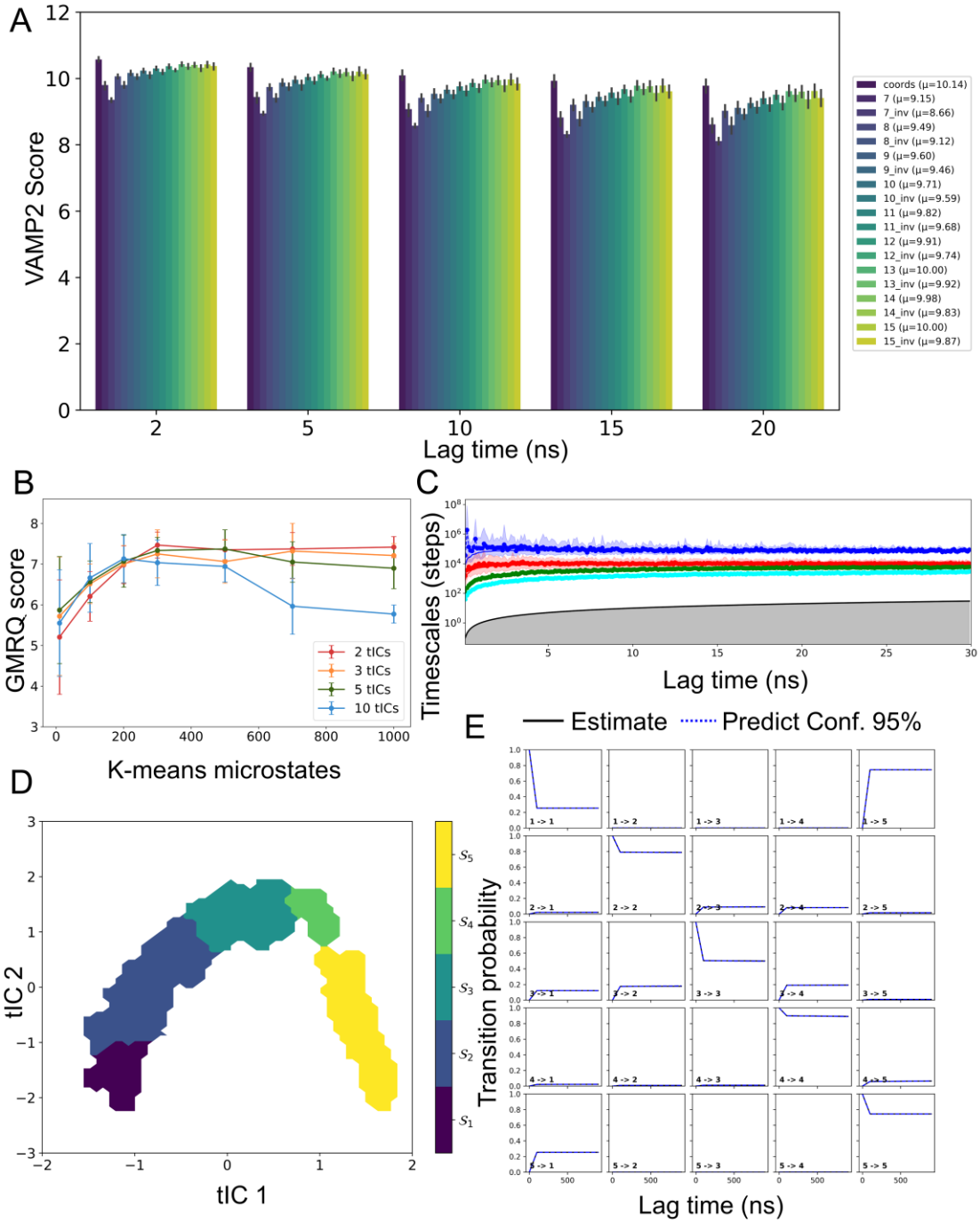

Supplementary Figure 3. The validation of an MSM constructed by tICA.

(A) The feature selection by calculating VAMP2 scores of the 10 slowest processes for a variety of features at varying lag times. The mean VAMP2 scores from 5-fold cross-validation are plotted as bar and standard deviations are plotted as error bars.

(B) The optimization of MSM hyperparameters by calculating GMRQ scores at varying numbers of tICs and microstates. The mean GMRQ scores from 5-fold cross-validation are plotted as dots and standard deviations are plotted as error bars.

(C) The results of the implied timescale test. Four distinct resolved timescales colored in blue, red, green, and cyan lines are shown as a function of lag time. The 95% confidence intervals for the eigenvalues are depicted as shaded areas. A black solid curve marks the boundary of a shaded region, indicating where the implied timescales fall short of the lag time.

(D) The distribution of 5 macrostates on the landscape. Corresponding colors are shown on the right.

(E) The results of the 5-state Chapman-Kolmogorov test. The probabilities of transiting between the macrostates (dash lines) observed in the simulations are consistent with the estimated probabilities from the constructed MSM (solid line).

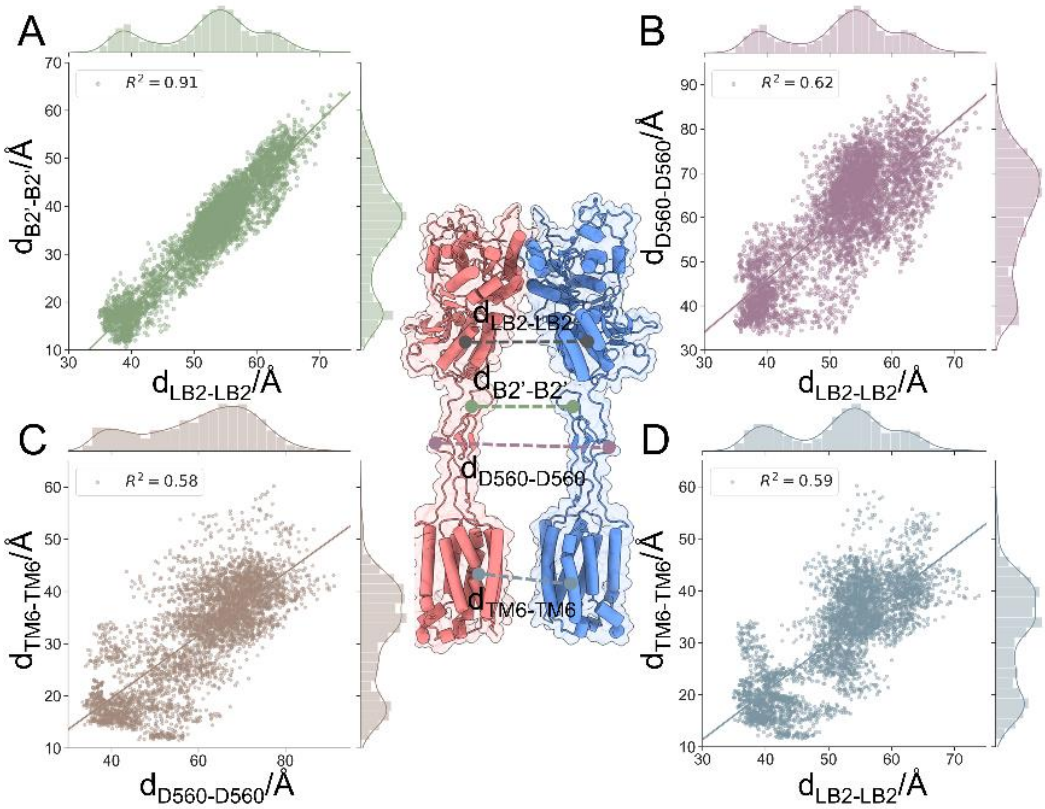

Supplementary Figure 4. Motion correlation between any two functional relevant domains.

The results include correlations between the VFT and the B2' module of CRDs (A), the VFT and the second A1 module of CRDs (B), the second A1 module of CRDs and the 7TM (C), the VFT and 7TM domains (D). The inter-domain dynamics between the VFT, the B2' module, the second A1 module of CRDs, and the 7TM domains are quantified by measuring the distance distributions between LB2-LB2 COM, B2'-B2' COM, D560-D560 Cα and TM6-TM6 COM, respectively. Scatter points represent simulation snapshots taken at 20 ns intervals.

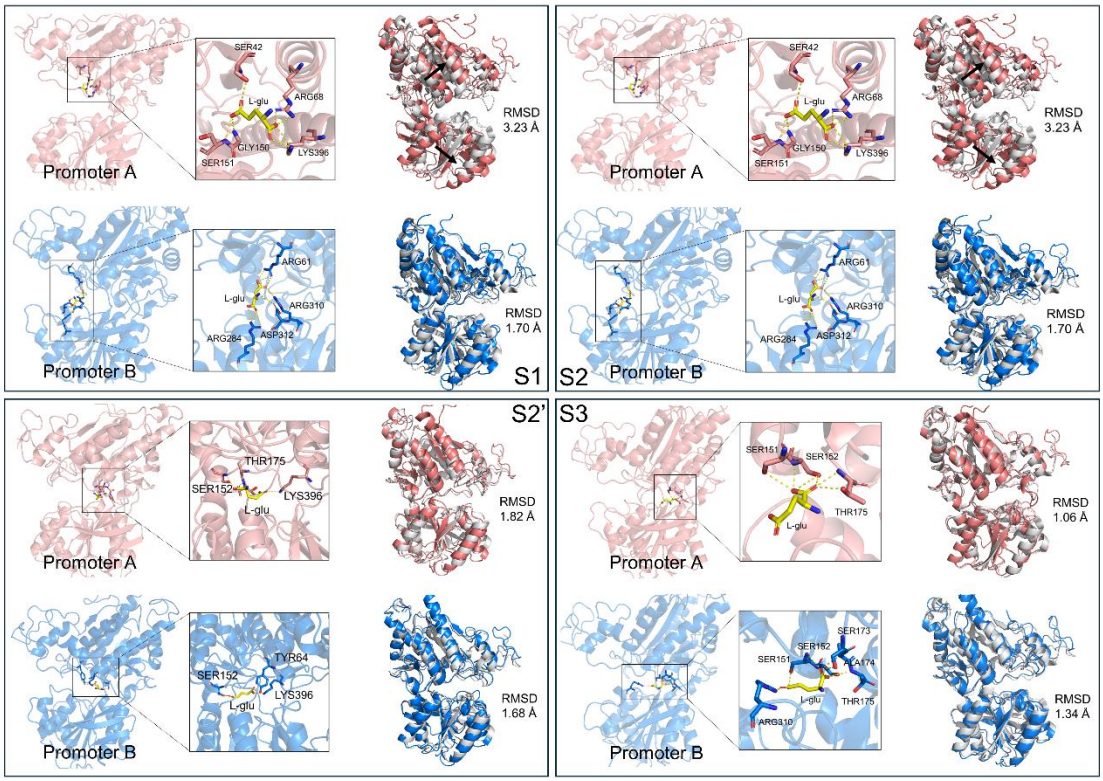

Supplementary Figure 5. Glutamate binding poses in the metastable states S1, S2, S2' and S3.

The left part of each panel presents the glutamate binding poses within protomer A and protomer B in both the overall and the enlarged view. The enlarged views emphasize the interactions between glutamate and the residues within the binding pocket. The engaged residues are represented as stick models, with yellow dotted lines illustrating hydrogen bonds. The right part shows the configuration of the VFT by measuring the Cα RMSD of the VFT of each protomer from the crystal VFT conformation (gray) in complex with glutamate (PDB:3LMK), denoted as $RMSD_{VFT}$.

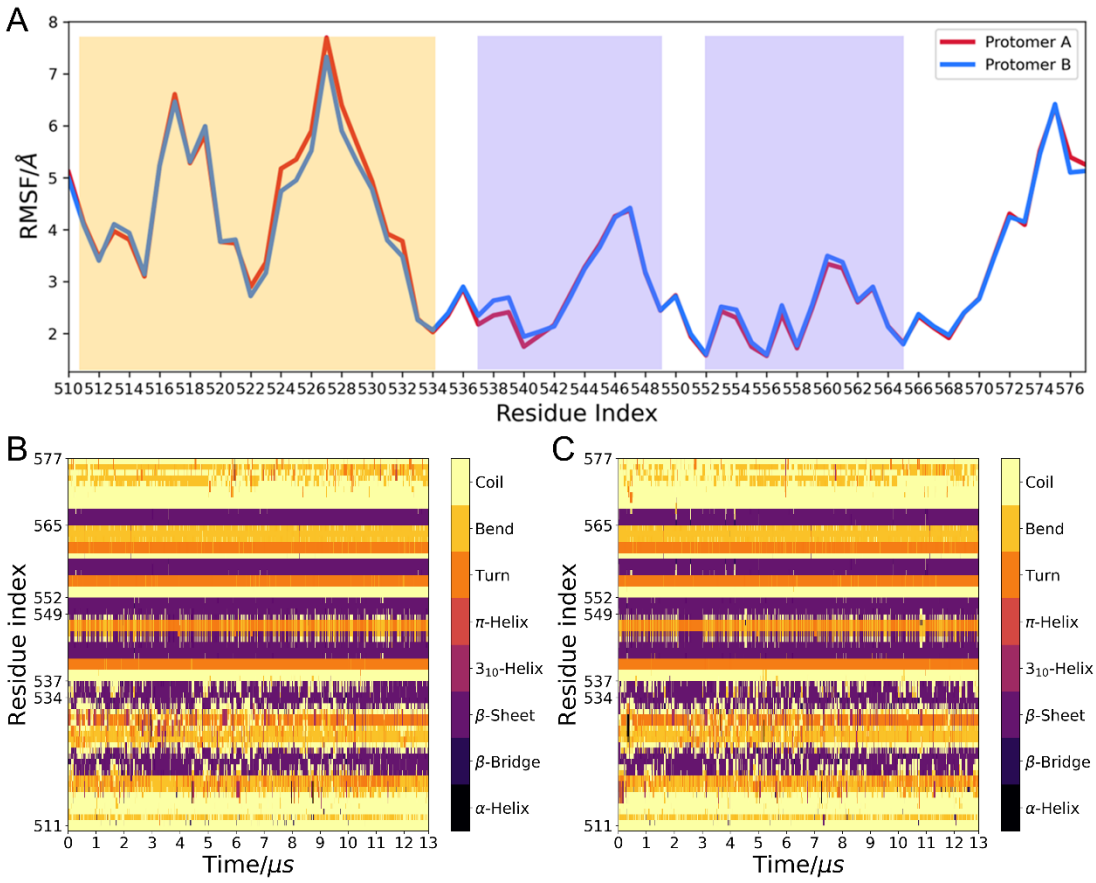

Supplementary Figure 6. CRD Conformational changes at each module.

(A) RMSFs of all heavy atoms of the CRDs. Both protomer A and protomer B exhibit similar fluctuation profiles.

(B, C) Secondary structure transitions of the CRDs within the promoter A (B) and promoter B (C), respectively. Each secondary structure category corresponding to its color is listed on the right.

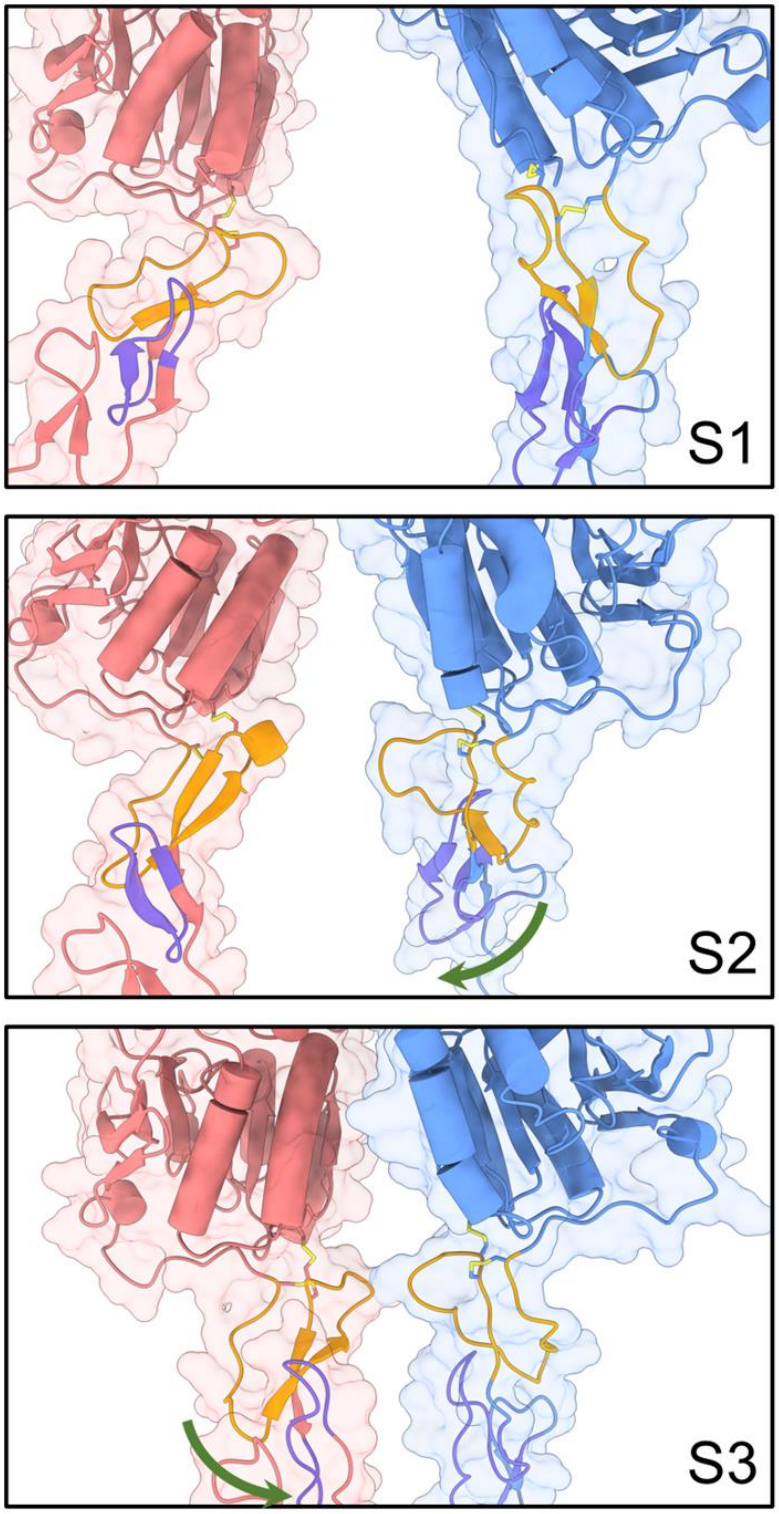

Supplementary Figure 7. Inter-domain arrangement of CRDs in the S1, S2 and S3. As the VFT of protomer B closes, the linked CRD coordinately moves, as indicated by the green arrow in S2. Subsequently, when the VFT of protomer A transitions to a closed state, the CRDs move closer to each other. Notably, the surface representation in S3 suggests that the B2' module is the first part to associate and form an interface.

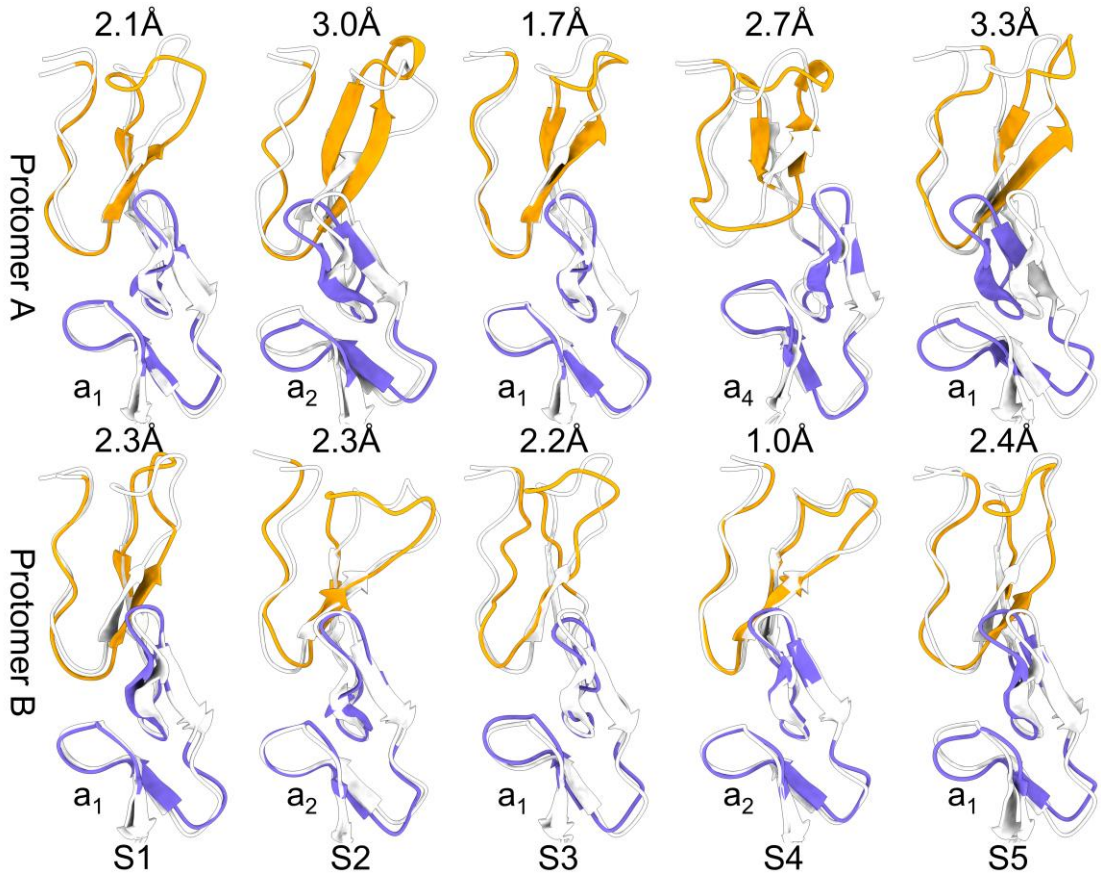

Supplementary Figure 8. The intra-domain conformation of CRD across the metastable states.

For each metastable state, protomers are aligned to the representative intra-domain CRD conformation that most closely matches, determined by the smallest Cα RSMD. The label for the corresponding representative intra-domain CRD conformation is positioned at the lower left of each structure, and the RMSD value is noted at the upper center.

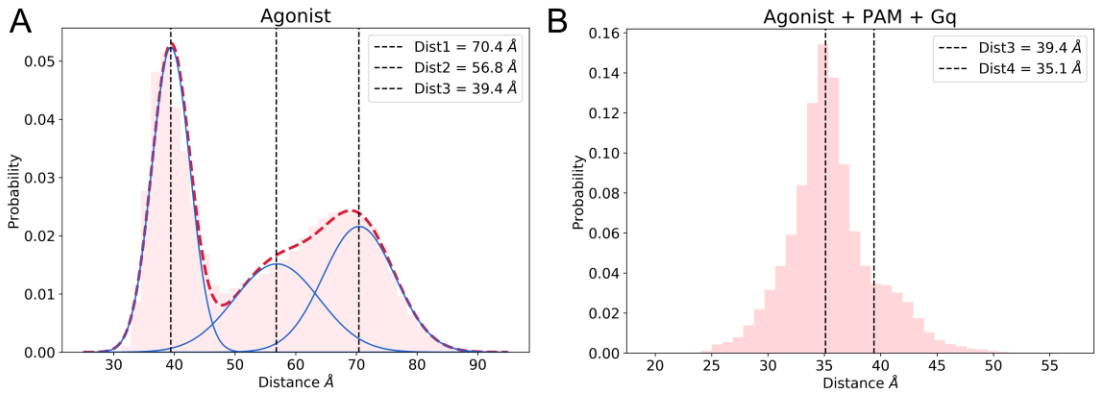

Supplementary Figure 9. Conformational distributions of $d_{D560\text{-}D560}$.

The red dashed line represents the overall distance distribution. Thin blue solid lines depict the Gaussian-fitted distributions of the three states upon only agonist loading (A) and the fully active state upon G_q coupling (B). These correspond to the four states identified in mGlu2, mGlu3 and mGlu5 through the smFRET technique, achieved by conjugating donor and acceptor fluorophores at analogous positions on the CRDs. In addition, the black dashed lines signify the means of each Gaussian-fitted distribution. Interestingly, the distribution showed that CRDs exhibited moderate inter-domain dynamics even in the inactive state of mGlu5. Consistently, in the apo inactive cryo-EM structure, the distance is 68.3 Å (PDB ID: 6N52). In the antagonist-bound inactive cryo-EM structure, the distance is 70.2 Å (PDB ID: 7FD9)[29]. In the CDPPB-bound inactive cryo-EM structure, the distance is 73.4 Å (PDB ID: 8T6J), which is close to the metastable state S1 (74.3 Å). This variability highlights the inherent flexibility within the CRDs, even in states traditionally considered inactive.

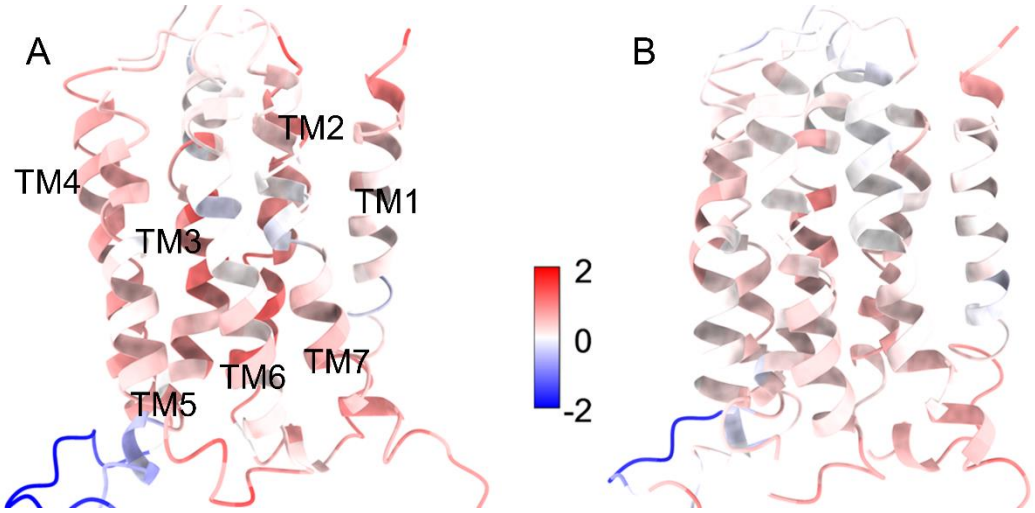

Supplementary Figure 10. Mappings of per-residue RMSD from MD simulations onto the structure of the 7TM domain.

The plots are for the protomer A (A) and protomer B (B), respectively. The per-residue RMSD is calculated from trajectories when the TM6-TM6 interface begins to form ($d_{TM6\text{-}TM6}$ < ~20 Å). The RMSD scales are shown in the middle and expressed in Å. The overall conformations of the 7M in both protomers exhibit fluctuations.

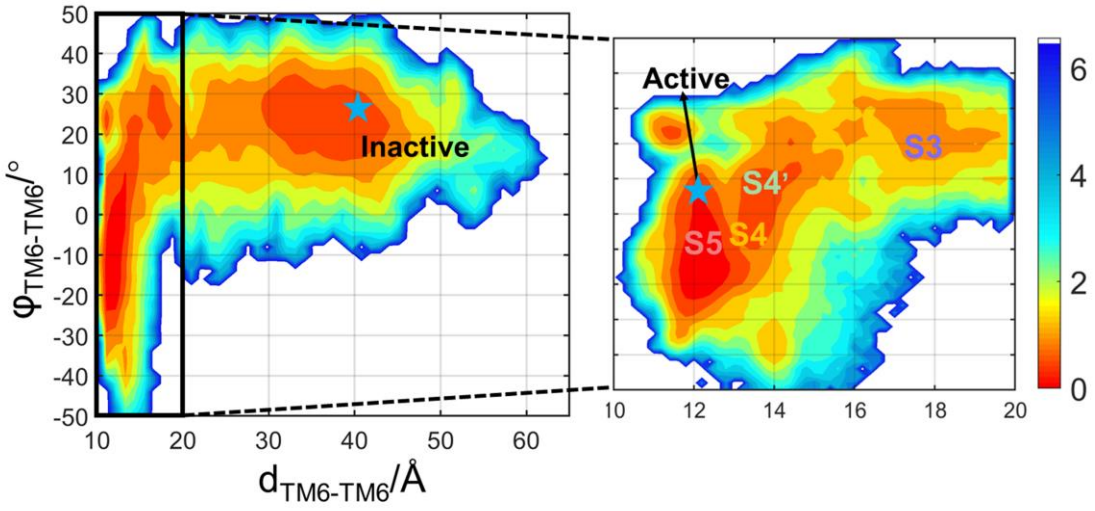

Supplementary Figure 11. Conformational landscape of the TM6-TM6 reorientation. This landscape is obtained by projecting all simulation trajectories onto $d_{TM6-TM6}$ and $\varphi_{TM6-TM6}$. The orientation of TM6-TM6 exhibits significant changes, transitioning from positive to negative dihedral, when the interface begins to form ($d_{TM6-TM6}$ < ~20 Å). The right portion of the Figure provides an enlarged view of this region, analogous to Figure 5B. The free energy scales are shown on the right and expressed in kcal/mol.

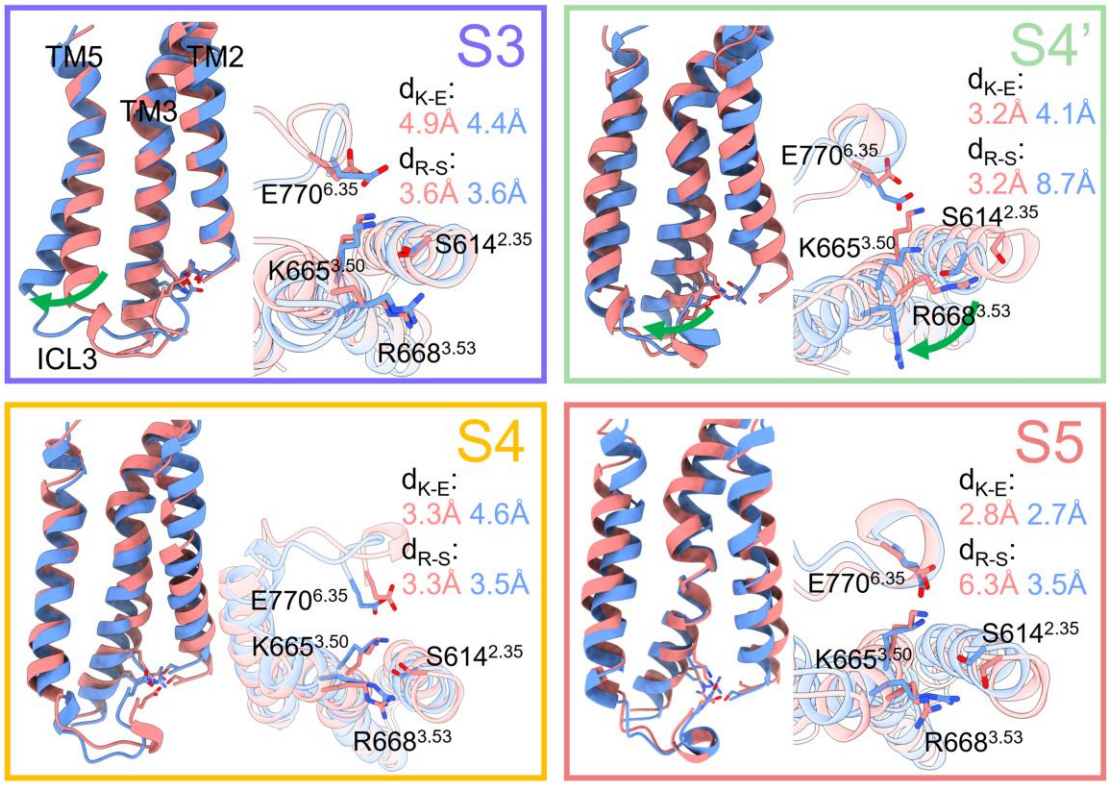

Supplementary Figure 12. The ionic-lock motifs in each metastable state during 7TM reorientation.

Each structure is presented within a box. The left half of the box offers a front view of TM2, TM3, and TM5, while the right half provides an elevated perspective on the 'ionic-lock' motif. In class A GPCRs, the salt bridge between $R^{3.50}$ and $E^{6.30}$ is regarded as a hallmark of the inactive state. A similar feature is observed in mGlu5, $K665^{3.50}$ forms a salt bridge with $E770^{6.35}$. Additionally, a less well-conserved $R668^{3.53}$ forms a hydrogen bond with $S614^{2.35}$ in ICL1, serving as a secondary lock to further stabilize the 7TM configuration. Critical residues are shown as sticks. The distance between $K665^{3.50}$ and $E770^{6.35}$ (d_{K-E}) is measured using the Nζ atom of K and the nearest Oε atom of E. The distance between $R668^{3.53}$ and $S614^{2.35}$ (d_{R-S}) is gauged using the Oγ atom of S and its closest Nη atom of R. The resulting distances are listed in the upper right. Protomer A is depicted in red, while protomer B is in blue.

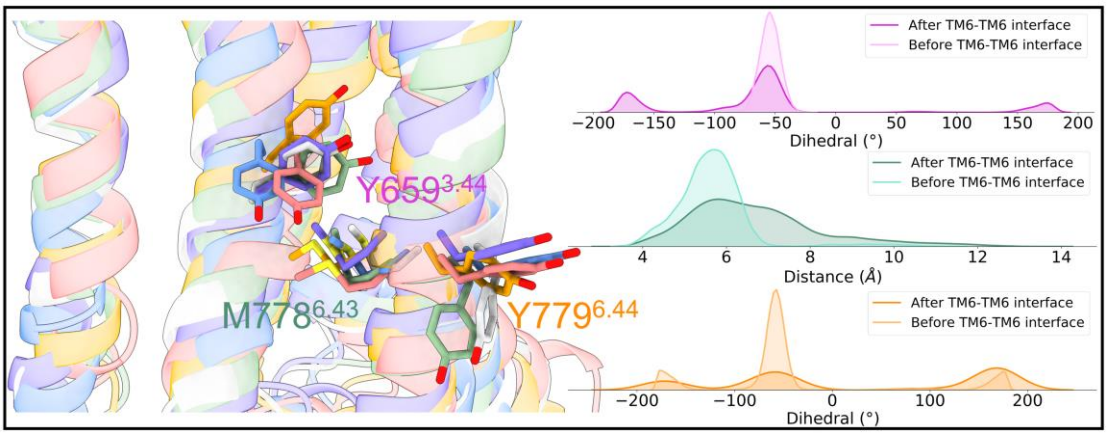

Supplementary Figure 13. Micro-switches conformation and dynamics of protomer A.

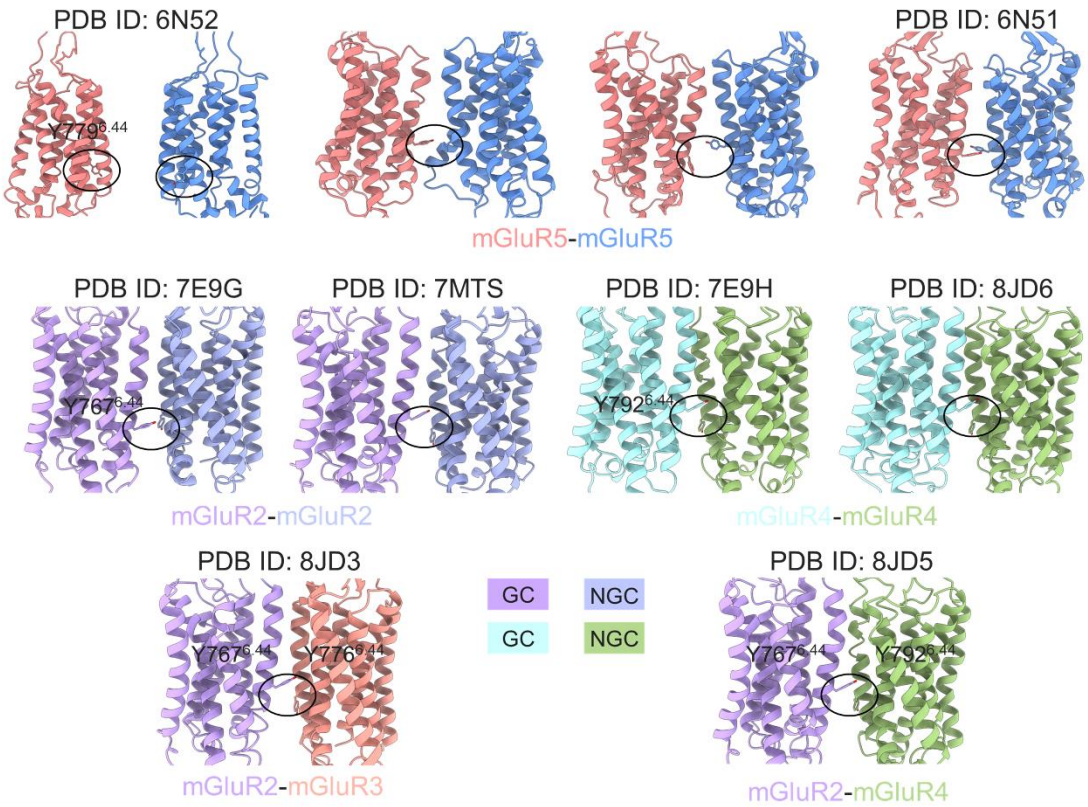

Supplementary Figure 14. Asymmetrical rotamer orientation of $Y^{6.44}$ across class C GPCRs.

The first row displays the asymmetrical rotamer conformation of $Y779^{6.44}$ along the mGlu5 homodimer activation process, as observed in our simulations (S3, S4' and S4). These asymmetrical changes are not observed in the crystal structures (6N51 and 6N52). The second row presents the asymmetrical orientation between G-protein-coupled (GC) and non-G-protein-coupled (NGC) protomer of $Y767^{6.44}$ in mGlu2 and $Y792^{6.44}$ in mGlu4 homodimer, as demonstrated in recently resolved structures. In newly available structures of Gi-attaching heterodimers, including mGlu2-mGlu3 and mGlu2- mGlu4, such an asymmetrical orientation of $Y^{6.44}$ is also evident.

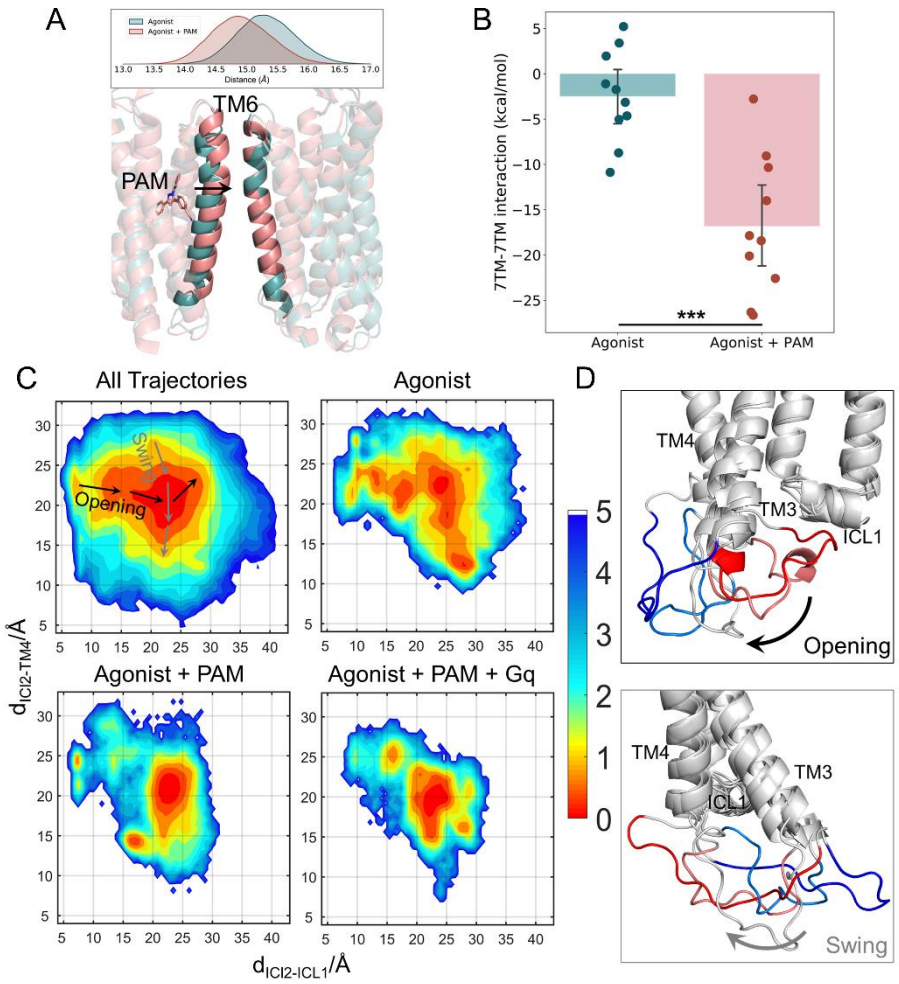

Supplementary Figure 15. Conformational changes upon CDPPB binding to the mGlu5.

(A) The CDPPB, glutamate-bound representative structure (red) exhibits notable proximity trends at the TM6-TM6 interface, as highlighted by the arrow, in comparison to the structure bound with glutamate alone (green). This observation is supported by the quantitative analysis of the distance distribution, specifically measured by the W785$^{6.50}$ Cα-Cα distance.

(B) The interaction free energy of the 7TMs (kcal/mol) was calculated using the MM/GBSA method. The data are presented as mean ± s.e.m. derived from ten independent MD simulations based on the agonist-bound structure (PDB ID: 6N51) and the agonist, PAM-bound structure (PDB ID: 8TAO). Statistical analysis of the differences between these two systems was conducted using a two-way ANOVA, followed by Dunnett's post hoc test ($P < 0.0001$).

(C) The conformational landscape of ICL2 derived from simulations. The *x*-axis ($d_{ICL2\text{-}ICL1}$) was defined as the distance between the Cα atom of C681 on the ICL2 and the center of mass (COM) of all Cα atoms of ICL1, reflecting the opening motion of ICL2 with increasing $d_{ICL2\text{-}ICL1}$ values. The *y*-axis ($d_{ICL2\text{-}TM4}$) was determined using the distance between the Cα atoms of C661 on the ICL2 and $C691^{4.30}$ on the TM4, the same points of the fluorescence experiments, representing the swinging motion of ICL2. The free energy scales of the landscape are shown on the right and are expressed in kcal/mol. (D) Representative structures of mGlu5, showcasing the varied conformations of ICL2.

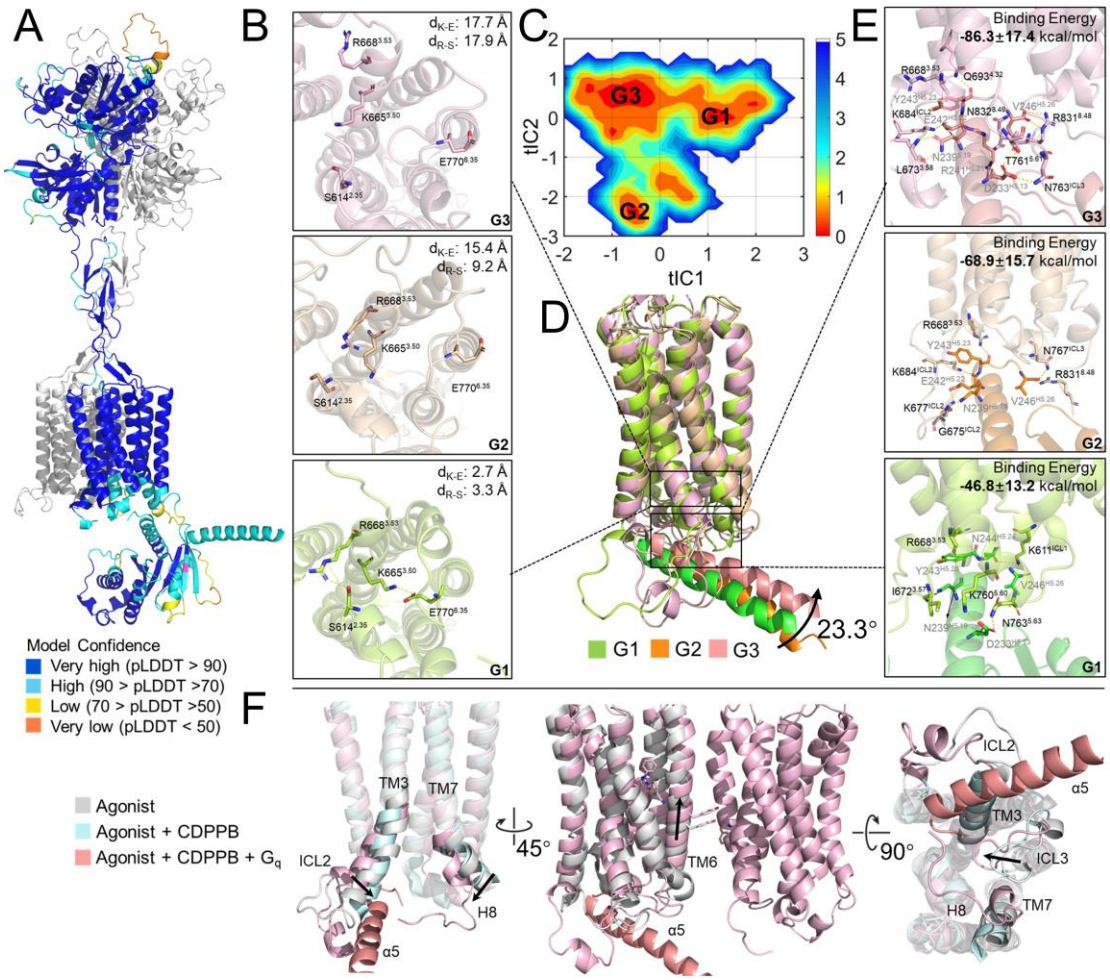

Supplementary Figure 16. Dynamics of the G_q coupling to mGlu5.

(A) Predicted mGlu5-G_q complex structure, color-coded by the predicted local distance difference test (pLDDT) score for evaluating model confidence.

(B) Illustration of 'ionic-lock' motifs in metastable states during G_q coupling. The distance between $K665^{3.50}$ and $E770^{6.35}$ ($d_{K\text{-}E}$) is measured from the Nζ atom of K and the closest Oε atom of E. The distance between $R668^{3.53}$ and $S614^{2.35}$ ($d_{R\text{-}S}$) is measured from the Oγ atom of S to the nearest Nη atom of R. Polar interactions are represented with yellow dashed lines.

(C) FEL derived from the first two tICs, with each local free energy minimum labeled by its corresponding metastable state. The free energy scales of the landscape are shown on the right and are expressed in kcal/mol.

(D) Representative mGlu5-G_q structures, showcasing the variety of G_q binding modes.

(E) The detailed interaction networks between mGlu5 and G_q, with binding free

energies calculated via the MM/GBSA method and summarized in the upper right corner.

(F) Comparison of the 7TM bundle from the CDPPB-bound protomer (PDB ID: 8TAO) and the agonist-bound protomer (PDB ID: 6N51) to that of the G_q-coupled protomer of G1. TM6 of the G_q-coupled protomer is noted for its tilt and shift of nearly half a helical pitch towards the extracellular side, resulting in an asymmetric TM6-TM6 interface. Arrows highlight the consequential conformational arrangement, particularly in the cytoplasmic end of TM3, intracellular loops (ICL2 and ICL3), and the H8 helix.

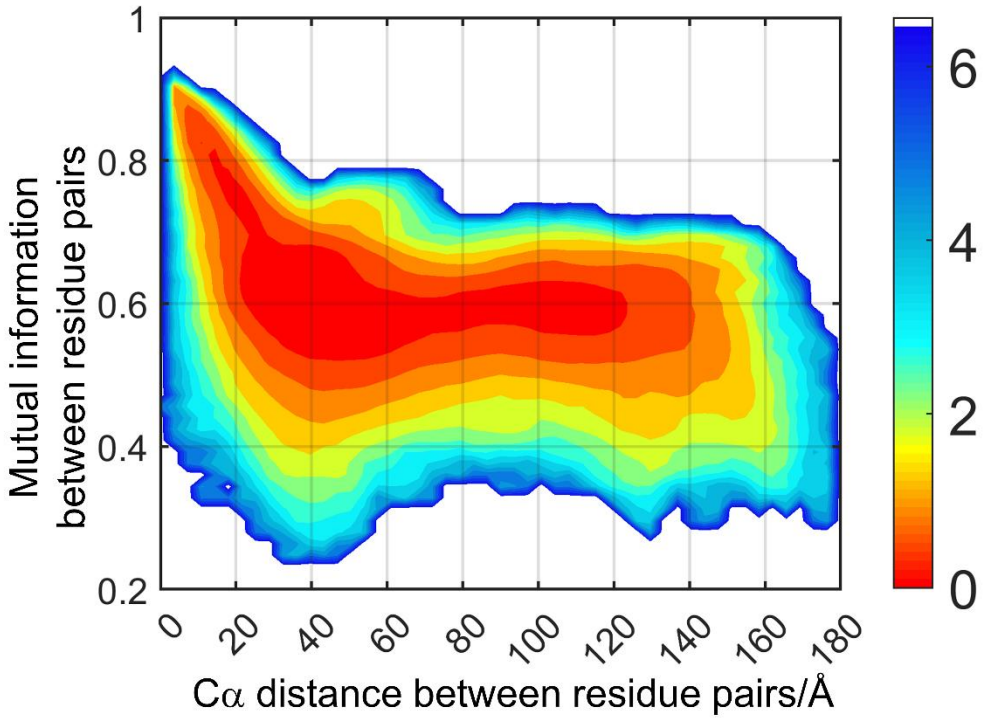

Supplementary Figure 17. Mutual information correlation among distant residue pairs. Variation of mutual information values between all the residue pairs in mGlu5 as a function of pairwise distance between their Cα atoms. It can be observed that main long-range communication (values within the area under 1 kcal/mol)) is predominantly within a Cα pairwise distance of 120 Å.

Supplementary Table 1. Summary of MD simulations performed on the various mGlu5 systems.

System	N_{atoms}	Simulation Length (ns)
Agonist-NEB image 1	177,468	1000 x 10
Agonist-NEB image 2	176,161	1000 x 10
Agonist-NEB image 3	191,758	1000 x 10
Agonist-NEB image 4	174,004	1000 x 10
Agonist-NEB image 5	176,201	1000 x 10
Agonist-NEB image 6	171,665	1000 x 10
Agonist-NEB image 7	200,700	1000 x 10
Agonist-NEB image 8	207,285	1000 x 10
Agonist-NEB image 9	227,043	1000 x 10
Agonist-NEB image 10	177,753	1000 x 10
Agonist-NEB image 11	180,396	1000 x 10
Agonist-NEB image 12	180,186	1000 x 10
Agonist-NEB image 13	179,078	1000 x 10
Agonist-PAM	205,844	1000 x 10
Agonist-PAM-G_q	286,947	1000 x 10

Supplementary Table 2. Sequence of all the primers used for site-directed mutagenesis.

Mutant	Sequence
I523C-F	TAAGGTGTGCAGGAAGGGAGAGGTGAGTTGCT
I523C-R	CCTTCCTGCACACCTTAATCTGCCCCTTCTCG
I523A-F	TAAGGTGGCAAGGAAGGGAGAGGTGAGTTGCT
I523A-R	CCTTCCTTGCCACCTTAATCTGCCCCTTCTCG
K521&V522&I523A-F	ATTGCCGCCGCCAGGAAGGGAGAGGTGAGTTGCT
K521&V522&I523A-R	TTCCTGGCGGCGGCAATCTGCCCCTTCTCGCATG
I523&R524&K525A-F	TTAAGGTGGCAGCAGCAGGAGAGGTGAGTTGCTGTTGGA
I523&R524&K525A-R	TGCTGCTGCCACCTTAATCTGCCCCTTCTCGC
$Y659^{3.44}$A-F	ATGTCCGCTTCAGCGCTCGTGACCAAAACCAA
$Y659^{3.44}$A-R	AGCGCTGAAGCGGACATGGCGGGAGACAGGCC
$M778^{6.43}$A-F	GCTTTTACCGCGTATACGACTTGTATAATCTGGCTGGC
$M778^{6.43}$A-R	CGTATACGCGGTAAAAGCAATATATTTGGCCTCA
$Y779^{6.44}$A-F	TACCATGGCTACGACTTGTATAATCTGGCTGGC
$Y779^{6.44}$A-R	CAAGTCGTAGCCATGGTAAAAGCAATATATTTGGCC

Supplementary Table 3. Glutamate-induced IP accumulation of WT and mutant mGlu5

Mutants	EC_{50} Ratio[1]	Span[2]		Expression[3]	
		% of WT	*P* value[4]	% of WT	*P* value
WT	1	100 ± 9	/	100 ± 9	/
I523C	/	107 ± 4	0.6358	97 ± 4	0.1536
I523A	0.8	73 ± 3**	0.0092	101 ± 6	0.6197
K521&V522&I523A	0.9	63 ± 3**	0.0047	104 ± 6	0.1554
I523&R524&K525A	0.4	36 ± 6***	0.0005	96 ± 5	0.0893
$Y659^{3.44}A$	5	63 ± 11**	0.0025	110 ± 17	0.2077
$M778^{6.43}A$	/	45 ± 11***	<0.0001	94 ± 7	0.3508
$Y779^{6.44}A$	/	64 ± 7**	0.0026	94 ± 6	0.8344

[1]The EC_{50} ratio (EC_{50}(Mutant)/EC_{50}(WT)) signifies the transition between the WT and mutant simulation dose curves and quantifies the effect of the mutations on mGlu5 signaling.

[2]The span is characterized as the interval between the maximum agonist response (Emax) and the vehicle.

[3] The expression levels of mGlu5 mutants are reported as percent compared to the WT from at least six independent measurements performed in technical duplicate.

[4]The statistical differences between WT and mutants were analyzed by one-way ANOVA followed by Dunnett's post-test (*P < 0.1, **P < 0.01, ***P < 0.001).

Supplementary Table 4. $\varphi_{TM6\text{-}TM6}$ across class C GPCR-G_i structures.

System[1]	PDB ID	$\varphi_{TM6\text{-}TM6}$[2]
mGlu2	7TMS	-2.6°
homodimer	7E9G	-14.3°
mGlu4	7E9H	-17.2°
homodimer	8JD6	-20.6°
mGlu2-mGlu3	8JD3	-2.3°
mGlu2-mGlu4	8JD5	-7.3°

[1]All the structures are in complex with G_i protein.
[2]$\varphi_{TM6\text{-}TM6}$ is defined by the Cα atoms of $E^{6.35A}$, $T^{6.60A}$, $T^{6.60B}$, $E^{6.35B}$.

S3. Supplementary References

1 Bergonzo, C., Campbell, A. J., de los Santos, C., Grollman, A. P. & Simmerling, C. Energetic preference of 8-oxoG eversion pathways in a DNA glycosylase. *J Am Chem Soc* **133**, 14504-14506, doi:10.1021/ja205142d (2011).

2 Li, H. *et al.* DNA Deformation-Coupled Recognition of 8-Oxoguanine: Conformational Kinetic Gating in Human DNA Glycosylase. *J Am Chem Soc* **139**, 2682-2692, doi:10.1021/jacs.6b11433 (2017).

3 Fallon, L. *et al.* Free Energy Landscapes from SARS-CoV-2 Spike Glycoprotein Simulations Suggest that RBD Opening Can Be Modulated via Interactions in an Allosteric Pocket. *J Am Chem Soc* **143**, 11349-11360, doi:10.1021/jacs.1c00556 (2021).

4 Dodd, T. *et al.* Polymerization and editing modes of a high-fidelity DNA polymerase are linked by a well-defined path. *Nat Commun* **11**, 5379, doi:10.1038/s41467-020-19165-2 (2020).

5 Lu, S. *et al.* Activation pathway of a G protein-coupled receptor uncovers conformational intermediates as targets for allosteric drug design. *Nat Commun* **12**, 4721, doi:10.1038/s41467-021-25020-9 (2021).

6 Li, H. J. *et al.* A structural and energetic model for the slow-onset inhibition of the Mycobacterium tuberculosis enoyl-ACP reductase InhA. *ACS Chem Biol* **9**, 986-993, doi:10.1021/cb400896g (2014).

7 McGibbon, R. T. & Pande, V. S. Variational cross-validation of slow dynamical modes in molecular kinetics. *J Chem Phys* **142**, 124105, doi:10.1063/1.4916292 (2015).

8 Westerlund, A. M. *et al.* Markov state modelling reveals heterogeneous drug-inhibition mechanism of Calmodulin. *Plos Comput Biol* **18**, e1010583, doi:10.1371/journal.pcbi.1010583 (2022).

9 Dror, R. O. *et al.* Activation mechanism of the beta2-adrenergic receptor. *Proc Natl Acad Sci U S A* **108**, 18684-18689, doi:10.1073/pnas.1110499108 (2011).
10 Manglik, A. *et al.* Structural Insights into the Dynamic Process of beta2-Adrenergic Receptor Signaling. *Cell* **161**, 1101-1111, doi:10.1016/j.cell.2015.04.043 (2015).
11 Liauw, B. W., Afsari, H. S. & Vafabakhsh, R. Conformational rearrangement during activation of a metabotropic glutamate receptor. *Nat Chem Biol* **17**, 291-297, doi:10.1038/s41589-020-00702-5 (2021).
12 Dror, R. O. *et al.* Pathway and mechanism of drug binding to G-protein-coupled receptors. *Proc Natl Acad Sci U S A* **108**, 13118-13123, doi:10.1073/pnas.1104614108 (2011).
13 Zhang, L. *et al.* Ligand-bound glutamine binding protein assumes multiple metastable binding sites with different binding affinities. *Commun Biol* **3**, 419, doi:10.1038/s42003-020-01149-z (2020).
14 Yu, A. & Lau, A. Y. Glutamate and Glycine Binding to the NMDA Receptor. *Structure* **26**, 1035-1043 e1032, doi:10.1016/j.str.2018.05.004 (2018).
15 Yu, A., Salazar, H., Plested, A. J. R. & Lau, A. Y. Neurotransmitter Funneling Optimizes Glutamate Receptor Kinetics. *Neuron* **97**, 139-149 e134, doi:10.1016/j.neuron.2017.11.024 (2018).
16 Cannone, G. *et al.* Conformational diversity in class C GPCR positive allosteric modulation. *bioRxiv*, 2023.2011.2007.565819, doi:10.1101/2023.11.07.565819 (2023).
17 Dogra, S. & Conn, P. J. Metabotropic Glutamate Receptors As Emerging Targets for the Treatment of Schizophrenia. *Mol Pharmacol* **101**, 275-285, doi:10.1124/molpharm.121.000460 (2022).
18 Stansley, B. J. & Conn, P. J. Neuropharmacological Insight from Allosteric Modulation of mGlu Receptors. *Trends Pharmacol Sci* **40**, 240-252, doi:10.1016/j.tips.2019.02.006 (2019).
19 Gregory, K. J. & Goudet, C. International Union of Basic and Clinical Pharmacology. CXI. Pharmacology, Signaling, and Physiology of Metabotropic Glutamate Receptors. *Pharmacol Rev* **73**, 521-569, doi:10.1124/pr.119.019133 (2021).
20 Miller, B. R., 3rd *et al.* MMPBSA.py: An Efficient Program for End-State Free Energy Calculations. *J Chem Theory Comput* **8**, 3314-3321, doi:10.1021/ct300418h (2012).
21 Krishna Kumar, K. *et al.* Stepwise activation of a metabotropic glutamate receptor. *Nature* **629**, 951-956, doi:10.1038/s41586-024-07327-x (2024).
22 Evans, R. *et al.* Protein complex prediction with AlphaFold-Multimer. *bioRxiv*, 2021.2010.2004.463034, doi:10.1101/2021.10.04.463034 (2022).
23 Jumper, J. *et al.* Highly accurate protein structure prediction with AlphaFold. *Nature* **596**, 583-589, doi:10.1038/s41586-021-03819-2 (2021).
24 Nehme, R. *et al.* Mini-G proteins: Novel tools for studying GPCRs in their active conformation. *PLoS One* **12**, e0175642, doi:10.1371/journal.pone.0175642 (2017).

25 Ling, S. *et al.* Structural insights into asymmetric activation of the calcium-sensing receptor–Gq complex. *Cell Research* **34**, 169-172, doi:10.1038/s41422-023-00892-2 (2024).
26 He, F. *et al.* Allosteric modulation and G-protein selectivity of the Ca2+-sensing receptor. *Nature* **626**, 1141-1148, doi:10.1038/s41586-024-07055-2 (2024).
27 Kato, H. E. *et al.* Conformational transitions of a neurotensin receptor 1-G(i1) complex. *Nature* **572**, 80-85, doi:10.1038/s41586-019-1337-6 (2019).
28 Nygaard, R. *et al.* The dynamic process of beta(2)-adrenergic receptor activation. *Cell* **152**, 532-542, doi:10.1016/j.cell.2013.01.008 (2013).
29 Nasrallah, C. *et al.* Agonists and allosteric modulators promote signaling from different metabotropic glutamate receptor 5 conformations. *Cell Rep* **36**, 109648, doi:10.1016/j.celrep.2021.109648 (2021).